Oxygen non-stoichiometry and electrical conductivity of $La_{0.2}Sr_{0.8}Fe_{0.8}B_{0.2}O_{3-\delta}$, B = Fe, Al, Ti, Ta

Ørjan Fossmark Lohne[a], Tor Grande[a], Martin Søgaard[b] and Kjell Wiik[a]

[a]Department of Materials Science and Engineering, Norwegian University of Science and Technology, NO-7491 Trondheim, Norway
[b]Department of Energy Conversion and Storage, Technical University of Denmark, Frederiksborgvej 399, DK-4000 Roskilde

Abstract

The oxygen non-stoichiometry was determined by coulometric titration for the perovskite oxides $La_{0.2}Sr_{0.8}FeO_{3-\delta}$ and $La_{0.2}Sr_{0.8}Fe_{0.8}B_{0.2}O_{3-\delta}$ (B = Al^{3+}, Ti^{4+} and Ta^{5+}) in the temperature range 600 °C $\leq T \leq$ 900 °C and the oxygen partial pressure range: $1 \cdot 10^{-15} \leq p_{O_2} \leq 0.209$ atm. The non-stoichiometry (δ) is observed to decrease with B-site substitution of Fe. The data can be well fitted with simple defect chemistry models. At low oxygen non-stoichiometry all compositions show a deviation from a localized electrons defect model. The standard and partial molar thermodynamic quantities were obtained and a gradual transition from localized to itinerant electrons with decreasing non-stoichiometry is proposed from the δ-dependency of the configurational entropy. The absolute value of the enthalpy of oxidation decreases upon B-site substitution of Fe proposing a decreased thermodynamic stability for the substituted materials. The electrical conductivity was measured at $T = 900$ °C in the oxygen partial pressure range: $1 \cdot 10^{-17} \leq p_{O_2} \leq 0.209$ atm. The electrical conductivity and charge carrier mobility decrease upon 20% substitution of Fe roughly by a factor of 2, but do not show a significant dependence on the nature of the B-site dopant.

1 Introduction

Mixed ionic and electronic conducting (MIEC) materials have attracted significant attention due to their potential use in applications such as oxygen gas separation membranes, electrodes for SOFC fuel cells and oxygen sensors [1]. These applications are characterized by "harsh" conditions such as high temperature, high pressure and both highly reducing and oxidising atmospheres. A key challenge, still to overcome, is the development of material systems showing sufficient stability at high temperatures and reducing conditions combined with adequate oxygen transport properties.

Materials with the perovskite structure, ABO_3, can withstand a high degree of oxygen vacancies yielding good oxygen transport properties as well as having a high electrical conductivity. They are therefore considered as a candidate material system for MIEC membranes [1, 2, 3]. The perovskite-type oxides $La_{1-x}Sr_xCoO_{3-\delta}$, $La_{1-x}Sr_xFeO_{3-\delta}$ and $La_{1-x}Sr_xFe_{1-y}Co_yO_{3-\delta}$ have all been shown to be promising materials for oxygen membranes [4, 5]. However, the chemical stability at reducing conditions is limited. The Co-containing materials have been shown to exhibit limited stability at low p_{O_2} [6, 7, 8] and $La_{1-x}Sr_xFeO_{3-\delta}$ is known to form the oxygen ordered brownmillerite structure at high strontium content and low p_{O_2} [9]. Partial substitution of iron in $La_{0.2}Sr_{0.8}FeO_{3-\delta}$ has shown to depress this ordering, maintaining the perovskite phase even at very reducing conditions [10]. By altering the composition with A and/or B-site substitution, both oxygen transport properties and chemical stability may be enhanced [8, 10, 11, 12].

In the research towards new and better MIEC materials, both electronic and oxygen transport, as well as thermodynamic, data are essential to properly understand the mechanisms governing the material properties and the effect of chemical composition. A wide range of studies have investigated the thermodynamic and electronic properties of the $La_{1-x}Sr_xFeO_{3-\delta}$ system, including systematic studies on the effect of strontium content [4, 13, 14, 15, 16, 17]. A few studies exist on effects of partial substitution of iron with Cr [18], Ga [19, 20] and Ti [21]. Systematic studies on the partial substitution of iron and the effect of the B-site dopant is however limited. In this study we investigate the system $La_{0.2}Sr_{0.8}Fe_{0.8}B_{0.2}O_{3-\delta}$ where B = Fe^{3+}, Al^{3+}, Ti^{4+} and Ta^{5+}. Iron is here substituted with B-site cations of increasing charge and ionic size. Coulometric titration was performed to determine the oxygen stoichiometry as function of partial pressure of oxygen and temperature. Thermodynamics of the point defect equilibria used to model the data were used to assess the thermodynamic stability of the solid solutions. The electronic transport properties of the materials were also investigated by conductivity measurements.

2 Experimental

LSFB powders were prepared by spray pyrolysis of aqueous precursors [10]. The powders were uniaxially pressed into cylindrical pellets and sintered at 1300 °C before crushed to $d_p \leq 10$ µm powder by a Retsch MM 2000 mixer mill. The crushed powders were re-annealed at 900 °C for 1 h and cooled at 50 K/h to obtain a homogeneous powder.

A schematic of the setup used for coulometric titration is shown in Fig. 1. Cylindrical samples of $Y_{0.16}Zr_{0.84}O_{1.92}$ (YSZ) were made by uni-axial pressing of powder in a 48 mm diameter die followed by cold isostatic pressing at $p = 325$ MPa. The green bodies were then machined to a disc and a cup before being sintered at 1550 °C. Typical dimensions of the sintered YSZ cups were (D×H) 22×12 mm outside and (d×h) 14×8 mm inside, giving a typical cell volume of 1.2 cm^3. On both the inner and outer surfaces of the cup, a ≈20 µm layer of YSZ/(La,Sr)MnO_3 was spray-

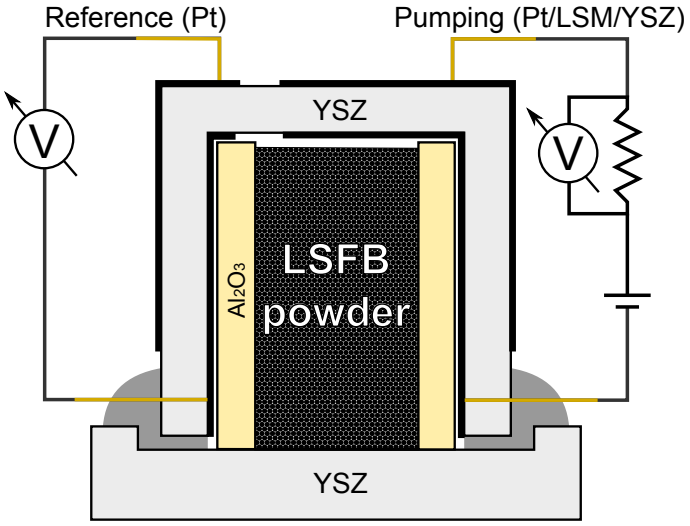

Fig. 1. A schematic of the coulometric titration setup.

painted on, serving as working electrodes after sintering at 1080 °C. Porous Pt was used as reference electrodes as well as current collector for the working electrodes. The porous Pt was hand-painted on the layers and sintered at 1000 °C. An alumina tube with outer diameter of 12.5 mm was placed on the YSZ disc to serve as a sample holder. To minimize the vacant volume of the cell, the height of the alumina tube was only marginally smaller than the height of the YSZ cup. Perovskite powder, typically 0.75-1 g was placed inside the alumina sample holder as illustrated in Fig. 1 and the YSZ cup was subsequently sealed with a glass paste (composition reported elsewhere [22]). The coulometric titration experiments were carried out in two parts. Part 1 was performed as stepwize changes in p_{O_2} in the region $10^{-16} \leq p_{O_2}$ [atm] ≤ 0.21 at 700 °C and 900 °C. The $\Delta\delta$ values were calculated by integrating the pumping current between two p_{O_2} steps and correcting for gas leakage. The magnitude of the leakage was determined as the current required to maintain a stable p_{O_2} inside the cup. The current used for the calculations of oxygen stoichiometry in the sample was obtained by subtracting the calculated leakage current from the measured current. Part 2 of the experiment was performed as a sequence of temperature cycles in the region $500 \leq T$ [°C] ≤ 900 where the potential of the reference electrode was continuously recorded. The temperature cycles were performed at open circuit conditions to ensure no transport of oxygen in or out of the cell. The volume of gas inside the cell is very small (≈ 0.3 cm^3) so the oxygen content in the sample material is much greater than the oxygen content of the gas in the cell volume. This allows δ to be considered constant during a temperature cycle. To ensure cell equilibrium at all times the cooling and heating rate were chosen as 15 K/h and 30 K/h, respectively, and the results were carefully examined for any hysteresis. The measurements were carried out simultaneously on up to four cells connected in parallel. At the end of the measurement, the samples were pumped down to $p_{O_2} \approx 10^{-16}$ atm for 24 h and cooled to room temperature.

Thermogravimetric analysis (TGA) was performed on powder samples to check the mass change as a function of temperature. The measurements were performed with

a Netsch STA 449C Jupiter simultaneous TG/DSC. The samples were heated up to 1000 °C at 50 K/h and cooled to room temperature at the same rate.

X-ray diffraction (XRD) measurements were performed to check phase purity before and after the coulometric titration using a Bruker D8 Focus.

Electrical conductivity was measured with a four-point DC method [23] on rectangular dense sintered samples of typical dimensions $1 \times 3 \times 20$ mm. The partial pressure of oxygen was controlled by a O_2/N_2 gas mixture for $p_{O_2} \geq 10^{-3}$ atm and a CO/CO_2 gas mixture for $p_{O_2} \leq 10^{-7}$ atm. The p_{O_2} was accurately determined by a YSZ oxygen sensor placed downstream of the sample chamber.

3 Theory

3.1 Coulometric titration

A coulometric titration setup consists of an electrochemical cell with an electronically insulating and oxygen ion conducting electrolyte. Yttria-stabilized Zirconia (YSZ) is often used as electrolyte and when a potential is applied over the cell, oxygen will be pumped through the electrolyte and in or out of the central compartment of the cell according to the reaction:

$$O_2(g) + 4\,e^- \rightleftharpoons 2\,O^{2-}(YSZ) \tag{1}$$

The difference in the oxygen chemical potential between the two electrodes of the cell is related to the applied voltage by the Nernst equation:

$$\mu_{O_2}^{in} - \mu_{O_2}^{out} = RT \ln\left(\frac{p_{O_2}^{in}}{p_{O_2}^{out}}\right) = zFV_{ref} \tag{2}$$

where $\mu_{O_2}^{in}$ and $\mu_{O_2}^{out}$ are the chemical potentials of oxygen in [J/mol] "inside", in the central glosed compartment (cf. Fig. 1), and outside the cell, respectively, R is the universal gas constant in [J/K · mol], T is the temperature in [K], $p_{O_2}^{in}$ and $p_{O_2}^{out}$ are the partial pressures of oxygen in [atm] inside and outside the cell respectively, z is the number of electrons transferred in the cell reaction ($z = 4$ for Eq. (1)), F is the Faraday constant in [C/mol] and V_{ref} is the voltage across the cell in [V]. The chemical potential of oxygen outside the cell can be expressed by the chemical potential of oxygen at the temperature T and standard pressure $p_{O_2}^0 = p_{tot}^0 = 1$ atm:

$$\mu_{O_2}^{out} = \mu_{O_2}^0(T, p_{O_2}^0) + RT \ln p_{O_2}^{out} \tag{3}$$

Hence Eq. (2) can be rewritten as:

$$\mu_{O_2}^{in} = \mu_{O_2}^0(T, p_{O_2}^0) + RT \ln p_{O_2}^{out} + 4FV_{ref} \tag{4}$$

For $p_{O_2}^{out} = 0.209$ atm, the quantity $\mu_{O_2}^0(T, p_{O_2}^0) + RT \ln p_{O_2}^{out}$ can be approximated with $23442\ \text{J/mol} - T \cdot 257.2\ \text{J/mol K}$. The partial pressure and chemical potential of oxygen inside the cell can then be calculated by Eq. (2) and (4), respectively.

According to Eq. (1), four electrons pumped through the external circuit correspond to one oxygen molecule pumped in or out of the central cell compartment. The flux of the oxygen can be expressed by the pumping current through Faraday's equation:

$$J_{O_2} = \frac{I}{4F} \tag{5}$$

When oxygen is pumped to or from the central cell compartment the chemical potential of oxygen inside the cell, $\mu^{in}_{O_2}$, will change and the powder sample will absorb or release oxygen to attain a new equilibrium with the current chemical potential ($\mu^{sample}_{O_2} = \mu^{in}_{O_2}$). The relative molar change in non-stoichiometry, $\Delta\delta$, from time t_1 to t_2 can then be expressed by:

$$\Delta\delta = \frac{2M}{m}\int_{t_1}^{t_2} J_{O_2}(t)dt = \frac{M}{2Fm}Q \tag{6}$$

where M is the molar mass of the sample in [g/mol], m is the mass of the powder sample in [g] and Q is the total amount of charge in [C] pumped to or from the cell. The potential change during a pumping session is monitored by the reference electrodes while the pumping current is measured over the external work circuit.

3.2 Defect model 1

The p_{O_2}-dependance of the oxygen non-stoichiometry for the $La_{1-x}Sr_xFeO_{3-\delta}$ system can be described with a simple point defect model [16]. The considered point defects are given in Table 1, using Kröger–Vink notation [24]. Here, the electronic defects

Table 1. Lattice host ions and point defects in Kröger-Vink notation considered in modelling the $La_{1-x}Sr_xFeO_{3-\delta}$ system.

A-site	*B-site*	*O-site*
La^{x}_{La} (La^{3+})	Fe^{x}_{Fe} (Fe^{3+})	O^{x}_{O} (O^{2-})
Sr'_{La} (Sr^{2+})	Fe'_{Fe} (Fe^{2+})	$V^{\bullet\bullet}_{O}$
	$Fe^{\bullet}_{Fe}$ (Fe^{4+})	

are assumed to be localized on iron sites as a change in oxidation state of iron from Fe^{3+} to Fe^{4+} and Fe^{2+} for holes and electrons, respectively. For the materials with partial substitution of iron, $La_{1-x}Sr_xFe_{1-y}B_yO_{3-\delta}$, an additional point defect is introduced, Ti'_{Fe} or Ta''_{Fe} for partial substitution by Ti^{4+} or Ta^{5+}, respectively. The B-site dopants are assumed to have fixed valency and the point defect model is established by assuming ideal solution of random non-interacting defects. The oxygen content in the sample depends on the partial pressure of oxygen in the surrounding gas. The incorporation of oxygen in the lattice can be described by the oxidation reaction:

$$\tfrac{1}{2}\,O_2(g) + V^{\bullet\bullet}_{O} + 2\,Fe^{x}_{Fe} = O^{x}_{O} + 2\,Fe^{\bullet}_{Fe} \tag{7}$$

The equilibrium constant for the oxidation reaction is given by:

$$K_{ox} = \frac{[\mathrm{O_O^x}][\mathrm{Fe_{Fe}^\bullet}]^2}{p_{\mathrm{O_2}}^{1/2}[\mathrm{V_O^{\bullet\bullet}}][\mathrm{Fe_{Fe}^x}]^2} = \frac{(3-\delta)[\mathrm{Fe_{Fe}^\bullet}]^2}{p_{\mathrm{O_2}}^{1/2}\delta[\mathrm{Fe_{Fe}^x}]^2} \tag{8}$$

An additional reaction might also occur as Fe^{3+} ions can undergo a charge-disproportionation into Fe^{2+} and Fe^{4+} ions, given by the reaction:

$$2\,\mathrm{Fe_{Fe}^x} = \mathrm{Fe_{Fe}'} + \mathrm{Fe_{Fe}^\bullet} \tag{9}$$

The equilibrium constant for the disproportionation reaction is given by:

$$K_D = \frac{[\mathrm{Fe_{Fe}^\bullet}][\mathrm{Fe_{Fe}'}]}{[\mathrm{Fe_{Fe}^x}]^2} \tag{10}$$

Mass conservation on the B-site and O-site can be expressed as:

$$[\mathrm{Fe_{Fe}^x}] + [\mathrm{Fe_{Fe}'}] + [\mathrm{Fe_{Fe}^\bullet}] = 1 - y \tag{11}$$

$$[\mathrm{V_O^{\bullet\bullet}}] + [\mathrm{O_O^x}] = 3 \tag{12}$$

where y corresponds to the concentration of the B-site dopant. Additionally, the electroneutrality condition provides the following equation:

$$[\mathrm{Sr_{La}'}] + [\mathrm{Fe_{Fe}'}] = \begin{cases} 2\,[\mathrm{V_O^{\bullet\bullet}}] + [\mathrm{Fe_{Fe}^\bullet}] & \text{(LSF)} \\ 2\,[\mathrm{V_O^{\bullet\bullet}}] + [\mathrm{Fe_{Fe}^\bullet}] + [\mathrm{Ti_{Fe}^\bullet}] & \text{(LSFTi)} \\ 2\,[\mathrm{V_O^{\bullet\bullet}}] + [\mathrm{Fe_{Fe}^\bullet}] + 2\,[\mathrm{Ta_{Fe}^{\bullet\bullet}}] & \text{(LSFTa)} \end{cases} \tag{13}$$

where $[\mathrm{Sr}'_{La}] = x = 0.8$ and $[\mathrm{Ti}^\bullet_{Fe}] = [\mathrm{Ta}^{\bullet\bullet}_{Fe}] = y = 0.2$. For simplicity, the following abbreviations will be used; $[\mathrm{Fe}^x_{Fe}] = a$, $[\mathrm{Fe}^\bullet_{Fe}] = p$, $[\mathrm{Fe}'_{Fe}] = n$ and $[\mathrm{V}^{\bullet\bullet}_O] = \delta$. Under highly oxidising conditions (high p_{O_2}) we have $a \gg n$ and $p \gg n$, hence Eq. (11) and Eq. (13) can be rewritten as

$$a + p = 1 - y \tag{14}$$

$$p = \begin{cases} 0.8 - 2\delta & \text{(LSF)} \\ 0.6 - 2\delta & \text{(LSFTi)} \\ 0.4 - 2\delta & \text{(LSFTa)} \end{cases} \tag{15}$$

The equilibrium constant for the oxidation reaction, Eq. (8), can then be rewritten and simplified to include only the measurable parameters δ and p_{O_2}:

$$K_{ox} = \frac{(3-\delta)p^2}{p_{O_2}^{1/2}\delta a^2} = \begin{cases} \frac{(3-\delta)(0.8-2\delta)^2}{p_{O_2}^{1/2}\delta(0.2+2\delta)^2} & \text{(LSF)} \\ \frac{(3-\delta)(0.6-2\delta)^2}{p_{O_2}^{1/2}\delta(0.2+2\delta)^2} & \text{(LSFTi)} \\ \frac{(3-\delta)(0.4-2\delta)^2}{p_{O_2}^{1/2}\delta(0.4+2\delta)^2} & \text{(LSFTa)} \end{cases} \tag{16}$$

From the electroneutrality condition, Eq. (13), we have when $n = p$:

$$\delta_{n=p} = \begin{cases} \frac{1}{2}[\mathrm{Sr}'_{La}] & = 0.4 \quad \text{(LSF)} \\ \frac{1}{2}([\mathrm{Sr}'_{La}] - [\mathrm{Ti}^{\bullet}_{Fe}]) & = 0.3 \quad \text{(LSFTi)} \\ \frac{1}{2}([\mathrm{Sr}'_{La}] - 2[\mathrm{Ta}^{\bullet\bullet}_{Fe}]) & = 0.2 \quad \text{(LSFTa)} \end{cases} \tag{17}$$

which corresponds to the average oxidation state of iron being equal to 3. From this, the equilibrium constant for the disproportionation reaction (K_D), Eq. (10), can be rewritten and simplified:

$$K_D = \frac{[\mathrm{Fe}^{\bullet}_{\mathrm{Fe}}][\mathrm{Fe}'_{\mathrm{Fe}}]}{[\mathrm{Fe}^{\mathrm{x}}_{\mathrm{Fe}}]^2} = \frac{np}{a^2} = \frac{p^2}{a^2} = \frac{K_{ox} p_{O_2}^{1/2} \delta}{3 - \delta} \tag{18}$$

3.3 Defect model 2

The defect model presented in section 3.2 have been reported to be insufficient to describe the defect chemistry for the material system $\mathrm{La}_{1-x}\mathrm{Sr}_x\mathrm{Fe}_{1-y}\mathrm{B}_y\mathrm{O}_{3-\delta}$ for low values of δ [19]. A different model has been used to explain the defect chemistry of the material where the previous model fails. This model, presented in this section, differs from the one presented in section 3.2 by assuming delocalized electronic defects. The incorporation of oxygen in the lattice can then be described by the oxidation reaction:

$$\tfrac{1}{2}\,\mathrm{O}_2(\mathrm{g}) + \mathrm{V}^{\bullet\bullet}_{\mathrm{O}} = \mathrm{O}^{\mathrm{x}}_{\mathrm{O}} + 2\,\mathrm{h}^{\bullet} \tag{19}$$

The equilibrium constant for this equation is given by:

$$K'_{ox} = \frac{[\mathrm{O}^{\mathrm{x}}_{\mathrm{O}}][\mathrm{h}^{\bullet}]^2}{p_{\mathrm{O}_2}^{1/2}[\mathrm{V}^{\bullet\bullet}_{\mathrm{O}}]} \tag{20}$$

The annihilation or formation of electronic charge carriers can be considered by the reaction:

$$0 = e' + h^{\bullet} \tag{21}$$

with the equilibrium constant given by:

$$K_e = [e'][h^{\bullet}] \tag{22}$$

The electroneutrality condition provides the following equation:

$$[\mathrm{Sr}'_{\mathrm{La}}] + [\mathrm{e}'] = \begin{cases} 2\,[\mathrm{V}^{\bullet\bullet}_{\mathrm{O}}] + [\mathrm{h}^{\bullet}] & \text{(LSF)} \\ 2\,[\mathrm{V}^{\bullet\bullet}_{\mathrm{O}}] + [\mathrm{h}^{\bullet}] + [\mathrm{Ti}^{\bullet}_{\mathrm{Fe}}] & \text{(LSFTi)} \\ 2\,[\mathrm{V}^{\bullet\bullet}_{\mathrm{O}}] + [\mathrm{h}^{\bullet}] + 2\,[\mathrm{Ta}^{\bullet\bullet}_{\mathrm{Fe}}] & \text{(LSFTa)} \end{cases} \tag{23}$$

where $[\mathrm{Sr}'_{La}] = x = 0.8$ and $[\mathrm{Ti}^{\bullet}_{Fe}] = [\mathrm{Ta}^{\bullet\bullet}_{Fe}] = y = 0.2$. Note that Model 1 simplifies to Model 2 if one sets $a = 1$.

3.4 Thermodynamics

For an ideal solution approach where all intrinsic defects and disorder are disregarded, the oxidation of a perovskite can be expressed by the general reaction [25]:

$$2\,\mathrm{ABO}_{2.5}(\text{Perovskite}) + \tfrac{1}{2}\,\mathrm{O}_2(\mathrm{g}) = 2\,\mathrm{ABO}_3(\text{Perovskite}) \tag{24}$$

The standard Gibb's energy of oxidation corresponding to this reaction is given by:

$$\begin{aligned}\Delta_{ox}G^0 &\equiv 2\Delta_f G^0(ABO_3) - 2\Delta_f G^0(ABO_{2.5}) \\ &= \Delta_{ox}H^0 - T\Delta_{ox}S^0 = RT\ln K\end{aligned} \tag{25}$$

where $\Delta_f G^0$ is the standard Gibb's energy of formation, $\Delta_{ox}H^0$ and $\Delta_{ox}S^0$ are the standard enthalpy and entropy of oxidation, respectively, and K is the equilibrium constant for the oxidation reaction. The configurational contribution of the oxidation of a perovskite can be included to obtain the partial molar thermodynamic quantities. For a localized electron model, the oxidation reaction is given in Eq. (7) and the partial molar Gibb's energy of oxidation is given by:

$$\mu_O^{LSFB} \equiv \Delta_{ox}G = \Delta_{ox}H - T\Delta_{ox}S = RT\ln\left(\frac{(3-\delta)[\mathrm{Fe}_{\mathrm{Fe}}^{\bullet}]^2}{p_{\mathrm{O}_2}^{1/2}\delta[\mathrm{Fe}_{\mathrm{Fe}}^{\mathrm{x}}]^2}\right) \tag{26}$$

where $\Delta_{ox}H$ and $\Delta_{ox}S$ are the partial molar enthalpy and entropy of oxidation, respectively. To avoid confusion it should be noted that the partial molar quantities are here defined with respect to per mol O(g) reacted, which correspond to per 1/2 mol O_2(g) reacted. By combining equation (2), (4), (8) and (25) and assuming equilibrium between the sample and the cell, $\mu_O^{LSFB} = \frac{1}{2}\mu_{O_2}^{in}$, we have:

$$\mu_O^{LSFB} = \frac{1}{2}\mu_{O_2}^0 + RT\ln\left(\frac{(3-\delta)[\mathrm{Fe}_{\mathrm{Fe}}^{\bullet}]^2}{\delta[\mathrm{Fe}_{\mathrm{Fe}}^{\mathrm{x}}]^2}\right) - \Delta_{ox}H^0 + T\Delta_{ox}S^0 \tag{27}$$

An expression for the partial molar entropy of oxidation at a given value of δ can then be obtained from Eq. (26)–(27):

$$\begin{aligned}\Delta_{ox}S &= -\left[\frac{\partial\mu_O^{LSFB}}{\partial T}\right]_\delta \\ &= -\frac{1}{2}\frac{\partial\mu_{O_2}^0}{\partial T} - \underbrace{R\ln\left(\frac{(3-\delta)[\mathrm{Fe}_{Fe}^{\bullet}]^2}{\delta[\mathrm{Fe}_{Fe}^{x}]^2}\right)}_{\text{configurational entropy}} - \Delta_{ox}S^0\end{aligned} \tag{28}$$

where the δ dependent term is labelled configurational entropy as introduced by Mizusaki et al. [26]. By combining Eqs. (26)–(28) the partial molar enthalpy of oxidation can be written:

$$\Delta_{ox}H = \frac{1}{2}\mu_{O_2}^0(T, P_A) - T\frac{1}{2}\frac{\partial\mu_{O_2}^0}{\partial T} - \Delta_{ox}H^0 \tag{29}$$

The configurational entropy term in Eq. (28) includes both the oxygen non-stoichiometry and the concentrations of Fe^{3+} and Fe^{4+}, hence for a localized electron model the configurational entropy is dependent on both the oxygen and iron sublattice.

For a delocalized electron model, the oxidation reaction is given in Eq. (19) and the partial molar Gibb's energy of oxidation is given by:

$$\Delta_{ox}G' = \Delta_{ox}H' - T\Delta_{ox}S' = RT\ln\left(\frac{3-\delta}{p_{\mathrm{O}_2}^{1/2}\delta}\right) \tag{30}$$

where the quantities are labelled with a prime to distinguish them from the quantities in Eqs. (26)–(29). The concentration of holes is here neglected from the configurational term as they are itinerant and thus the configuration of the lattice is independent on the concentration of holes. Following the same steps as above, the partial molar entropy of oxidation then becomes:

$$\Delta_{ox}S' = -\frac{1}{2}\frac{\partial\mu^0_{O_2}}{\partial T} - \underbrace{R\ln\left(\frac{3-\delta}{\delta}\right)}_{\text{configurational entropy}} - \Delta_{ox}S^0 \tag{31}$$

The electrons and holes are now itinerant and thus do not have a configurational contribution to the lattice. Hence, the configurational term is only determined by the oxygen sublattice.

4 Results and discussion

4.1 X-ray diffraction

The X-ray diffractograms recorded at room temperature of the powder samples before and after coulometric titration measurements are shown in Fig. 2. All the materials were shown to be single phase cubic perovskites before the coulometric titration measurements. The LSF sample did not show any trace of a decomposed perovskite phase after the coulometric titration but was identified as an orthorombic brownmillerite phase. LSF is known to transform into an ordered brownmillerite phase at low p_{O_2} and this has also been shown in a previous report [10]. LSFTi and LSFTa remained a single phase cubic perovskites after the coulometric titration experiment, hence all the materials are found to be stable down to the lowest partial pressure of oxygen during the measurement, $p_{O_2} \approx 10^{-16}$ atm at 900 °C. The molar volume and lattice parameters determined by refinement of the XRD measurements are summarized in Table 2.

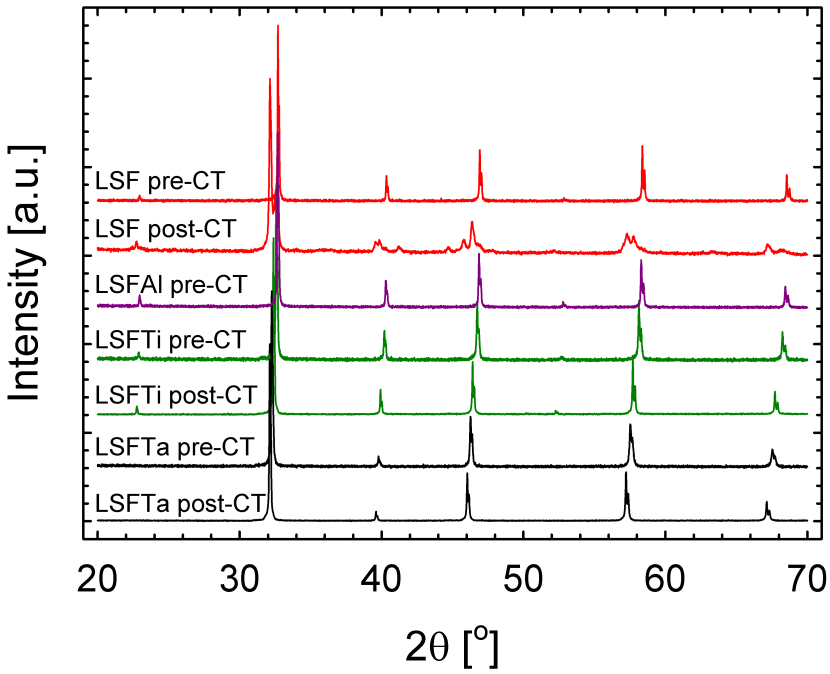

Fig. 2. X-ray diffracograms of the materials before and after coulometric titration.

Table 2. Crystal structure parameters at 298 K before and after coulometric titration measurements and ionic radii (IR) for different cations [27].

Sample		*Structure*	*a* [Å]	*b* [Å]	*c* [Å]		B^{n+}	*IR* [Å]
LSF	pre CT	Cub.	3.867	-	-		Fe^{4+}	0.585
LSFAl	pre CT	Cub.	3.874	-	-		Al^{3+}	0.535
LSFTi	pre CT	Cub.	3.883	-	-		Ti^{4+}	0.605
LSFTa	pre CT	Cub.	3.919	-	-		Ta^{5+}	0.64
LSF	post CT	Orth.	5.500	11.89	5.566		Fe^{3+}(HS)	0.645
LSFTi	post CT	Cub.	3.913	-	-			
LSFTa	post CT	Cub.	3.941	-	-			

4.2 Coulometric titration and TGA

The recorded V_{ref} as a function of temperature for LSF, obtained from the temperature sweep cycles (see section 2, is presented in Fig. 3. The data obtained at low temperatures and p_{O_2} are not reproduced in Fig. 3 due to some hysteresis and a non-linear V_{ref} vs. temperature curve. The hysteresis and non-linearity is attributed to a poor performing reference electrode at low p_{O_2} and temperature. The hysteresis between heating and cooling runs for the presented data is very low (≤ 1 mV). This clearly shows that the cell is gas tight and the sample is in equilibrium with the gas inside the cell at all times. The change in δ during a temperature cycle was less than 0.01 % and the amount of oxygen exchanged with the sample is therefore negligible and δ is regarded as constant throughout the temperature cycle. Values of δ vs. p_{O_2} at different temperatures were obtained by interpolating data points from the data presented in Fig. 3. The measured oxygen non-stoichiometries for LSF, LSFTi and LSFTa as a function of $\log(p_{O_2})$ at different temperatures are shown in Fig. 4, where the data points obtained from the temperature cycles are shown as open symbols. The data obtained by performing stepwise changes in p_{O_2} are shown as solid symbols. Very good agreement between the two measurement methods is observed. The leakage current was found to be typically $I_{leak} \approx 5 \cdot 10^{-6} \times \log(p_{O_2}) + 5 \cdot 10^{-6}$ A at 900 °C. To obtain the absolute values for the non-stoichiometry, we assume the situation where $n = p$ to correspond to the inflection point of δ vs. p_{O_2} at 900 °C in Fig. 4. The absolute value of the oxygen non-stoichiometry have then been determined by letting Eq. (17) be valid at $\frac{d^2\delta}{d(\log p_{O_2})^2} = 0$ of a 3-degree polynomial fit to the data. The solid lines in Fig. 4 correspond to the best results of a least-square-fit of

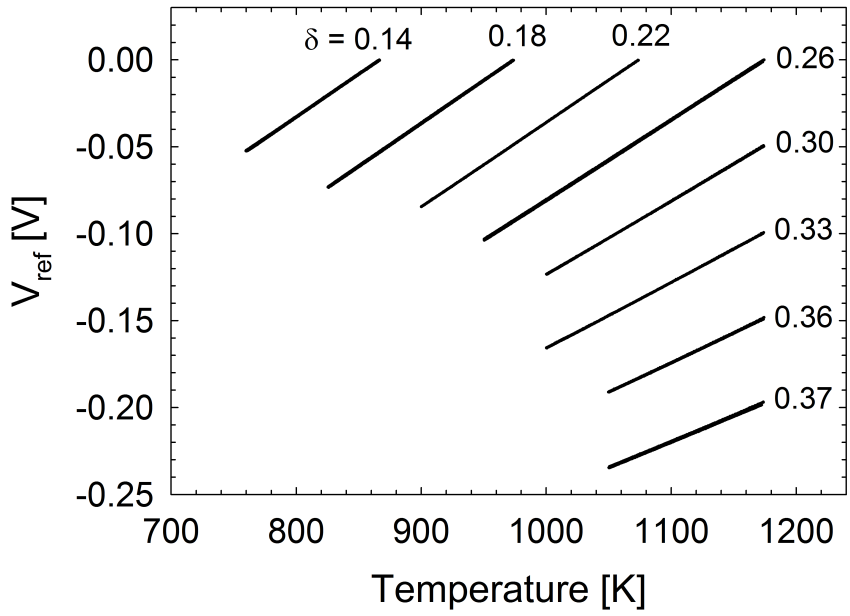

Fig. 3. V_{ref} as a function of temperature for LSF recorded during temperature cycles. The numbers show the constant δ value for each cycle.

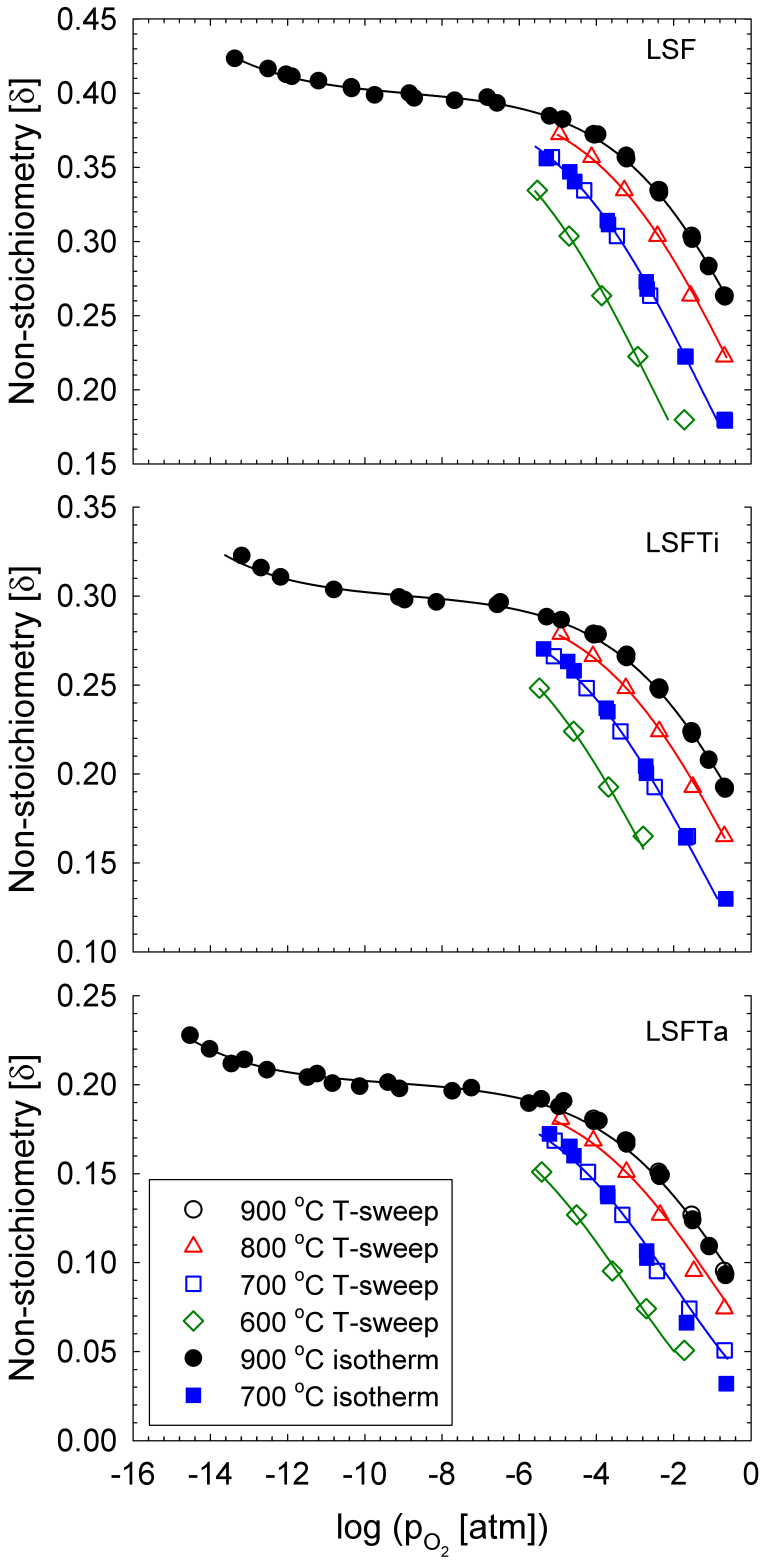

Fig. 4. Oxygen non-stoichiometry as a function of p_{O_2} at different temperatures. Open symbols are data points obtained from temperature cycles and closed symbols are obtained from p_{O_2} steps at constant temperature. The solid lines are fits to the point defect model 1 described in section 3.2.

the data to the defect model described in section 3.2 (model 1). The fits for data at 900 °C were obtained by simultaneously solving for Eq. (8) and Eq. (10) where the equilibrium constants, K_{ox} and K_D, calculated from Eq. (16) and Eq. (18), respectively, have been used as initial values for the fitting. The data at $T \neq 900$ °C are limited to p_{O_2} higher than the inflection point and the fits were obtained using the simplified Eq. (16). The modelled non-stoichiometry fit well with the experimental data for LSF and LSFTi while there is a small deviation for LSFTa at low δ values suggesting some deviation from ideality. This will be treated further in section 4.3.

The oxygen non-stoichometry as a function of temperature was also measured by TGA. The data are shown in Fig. 5 where they are also compared with the values obtained from coulometric titration. The coulometric titration data at 900 °C have been used as reference points. The TGA curves fit well with the coulometric titration data points in the measured temperature range. The apparent hyperstoichiometry at room temperature for LSFTa is assigned to an experimental deviation as oxygen interstitials are highly unlikely to form at these low temperatures. LSFTa is therefore regarded as stoichiometric ($\delta \approx 0$) at room temperature. The oxygen non-stoichiometry $(3-\delta)$ for LSF and LSFTi at room temperature is 2.96 and 2.97, respectively. The equilibrium constants obtained from the fitting of the coulometric titration data shown in Fig. 4 are presented in Table 3. Mizusaki et al. [4] have reported K_{ox} and K_D for $La_{1-x}Sr_xFeO_{3-\delta}$ ($0.1 \leq x \leq 0.6$) which are presented in

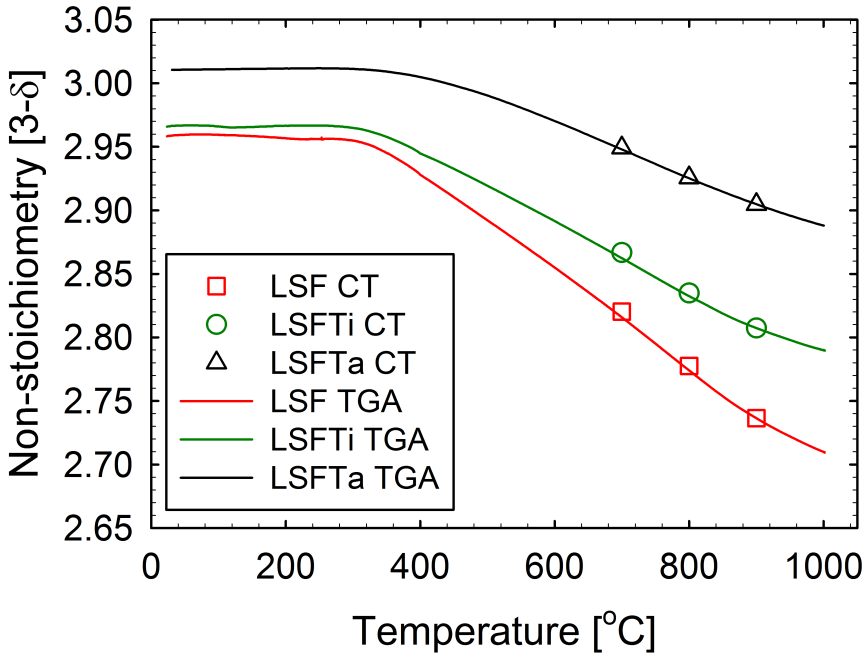

Fig. 5. Oxygen non-stoichiometry as a function of temperature obtained from coulometric titration (CT) and thermogravimetric analysis (TGA) in air. The CT data points at 900 °C have been used as reference points to calculate the non-stoichiometry from the TGA measurement.

Fig. 6 together with data from this study. The data from Mizusaki et al. show a linear $\log K_{ox}$ and $\log K_D$ relationship with the strontium content, x. Following this relationship, predicted values for K_{ox} and K_D for $x = 0.8$ at 900 °C are 2.8 and $2.4 \cdot 10^{-5}$, respectively. The data for $La_{0.2}Sr_{0.8}FeO_{3-\delta}$ in this study fit very well into this linear relationship.

Table 3. Equilibrium constants at different temperatures.

	K_{ox} [atm^{-1}]				K_D
	900 °C	800 °C	700 °C	600 °C	900 °C
LSF	3.1	8.0 ± 0.3	27 ± 1	115 ± 6	1.7e-5
LSFTi	4.1	10.0 ± 0.4	32.9 ± 0.7	135.1 ± 0.9	1.7e-5
LSFTa	7.5	15 ± 2	51 ± 4	210 ± 14	1.2e-5

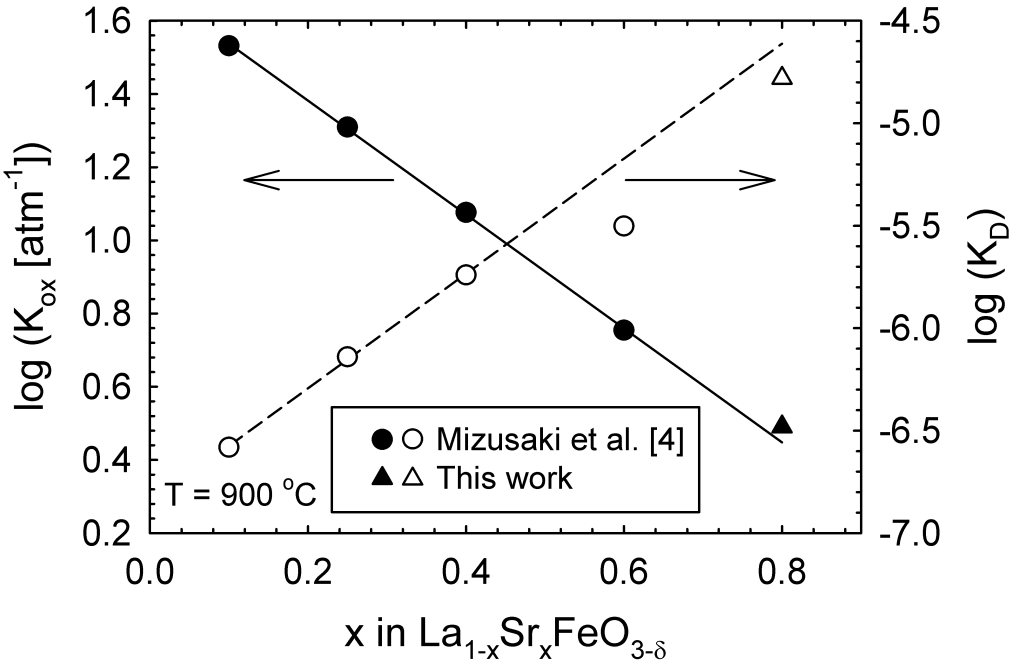

Fig. 6. K_{ox} (closed symbols) and K_D (open symbols) at 900 °C for $La_{1-x}Sr_xFeO_{3-\delta}$ as a function of strontium content, x. Circle symbols taken from Mizusaki et al. [4] and triangle symbols from this study. The solid line is a linear fit to K_{ox} for $x \leq 0.6$ and the broken line is a linear fit to K_D for $x \leq 0.4$.

The difference in K_{ox} between compositions (cf. Table 3) is quite large due to the large difference in δ-value between the compositions. However, the B-site substitution does not significantly influence the disproportionation reaction, determined by K_D. A similar result has also been shown for Ga-doped LSF by Yoo et al. [20].

When partially substituting iron with an aliovalent cation, the extra charge introduced in the material must be compensated to fulfil the electroneutrality condition, Eq. (13), either by a change in concentration of oxygen vacancies, by a change in the concentration of Fe^{2+} and/or Fe^{3+} or a combination of the two. This is referred to as ionic or electronic compensation, respectively. At low temperatures the difference in oxygen non-stoichiometry is small, as shown in Fig. 5, and electronic compensation is the main mechanism. At high temperatures, the shape of the δ versus p_{O_2} curves (see Fig. 7 (a)), is quite similar for all the samples investigated, hence there is a large difference in the concentration of oxygen vacancies, δ, throughout the whole measurement range. This suggests that ionic compensation is the dominating charge compensation mechanism for B-site substituted LSF at high temperatures. The average iron oxidation state is shown as a function of p_{O_2} at 900 °C in Fig. 7 (b). One can see that the average oxidation state of iron is found to be independent of the nature of the B-site dopant. The insert in Fig. 7 (b) shows the calculated concentrations of Fe^{2+} (n), Fe^{3+} (a) and Fe^{4+} (p) as a function of p_{O_2}. Only small differences in a and n are apparent while p is close to equal between the compositions. This suggests that electronic compensation is negligible at high temperatures for the B-site substituted LSF compositions investigated here.

4.3 Thermodynamics

The temperature dependency of the chemical potential of oxygen in the sample, $\mu_{O_2}^{LSFB}$, at constant δ was calculated from the cell voltage, V_{ref}, obtained from the temperature cycles shown in Fig. 3, assuming $\mu_O^{LSFB} = \frac{1}{2}\mu_{O_2}^{in}$. The partial molar enthalpy and entropy of oxidation was then obtained by the coefficients of a linear fit to μ_O^{LSFB} vs. $1/T$ according to Eq. (26). The obtained values of $\Delta_{ox}S$ and $\Delta_{ox}H$ are shown in Fig. 8 (a) and (b), respectively. The data for $\delta \geq 0.26/0.19/0.09$ for LSF/LSFTi/LSFTa have been obtained from temperature cycles starting at 900 °C, while the data for lower δ have been obtained from temperature cycles starting at 800, 700 and 600 °C, respectively. The data for LSFAl have been obtained from temperature cycles starting at 900 °C. The glass seal of the LSFAl sample broke during measurements and additional measurements were not obtained for this composition. Hence, the absolute non-stoichiometry of LSFAl is unknown and the data in Fig. 8 are presented assuming the average oxidation state of LSFAl at 900 °C being close to equal with the three other compositions according to the data presented in Fig. 7 (b). The solid lines in Fig. 8 (a) are calculated from Eq. (28) (model 1), using the relations given in Eq. (14) and (15), and represents the $\Delta_{ox}S$ dependency on δ arising from the configurational entropy term in Eq. (28). At high oxygen non-stoichiometries this dependency fits well with the experimental data, while at lower values of δ there is a misfit between the calculated $\Delta_{ox}S$ and the experimentally obtained values.

The calculated partial molar enthalpy of oxidation ($\Delta_{ox}H$), shown in Fig. 8 (b), is nearly constant at high oxygen non-stoichiometry, which supports the ideal solution approximation used in the point defect model. At lower δ values the enthalpy is

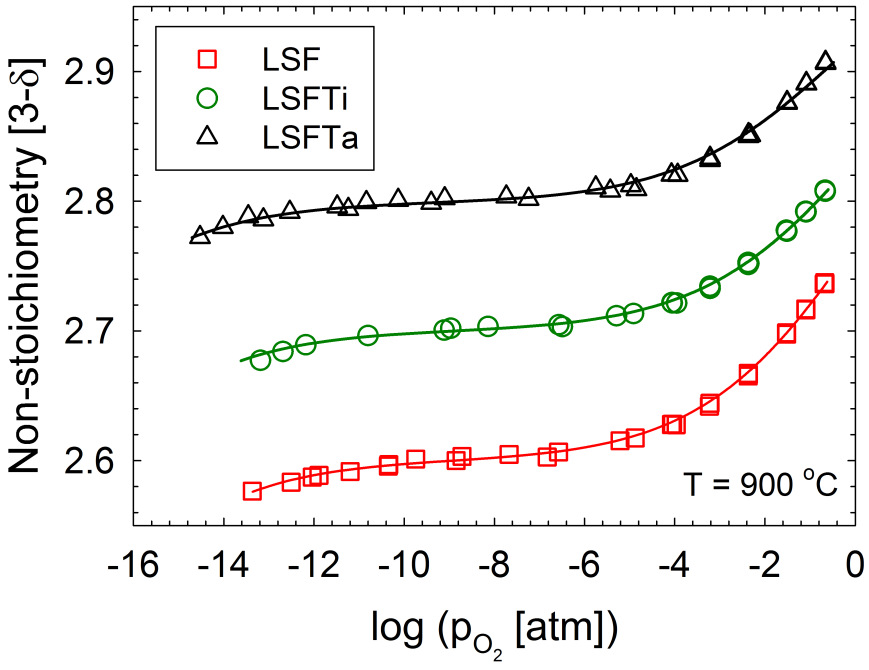

(a)

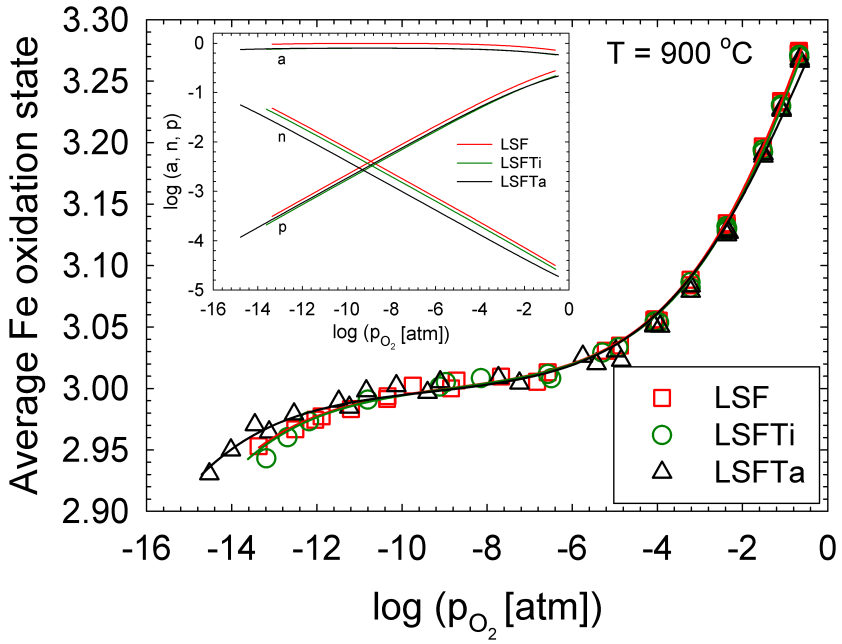

(b)

Fig. 7. (a) Oxygen non-stoichiometry and (b) average oxidation state of iron as a function of p_{O_2} at 900 °C. The solid lines are fits to the point defect model 1 described in section 3.2. The insert in (b) shows the concentration of Fe^{2+} (n), Fe^{3+} (a) and Fe^{4+} (p).

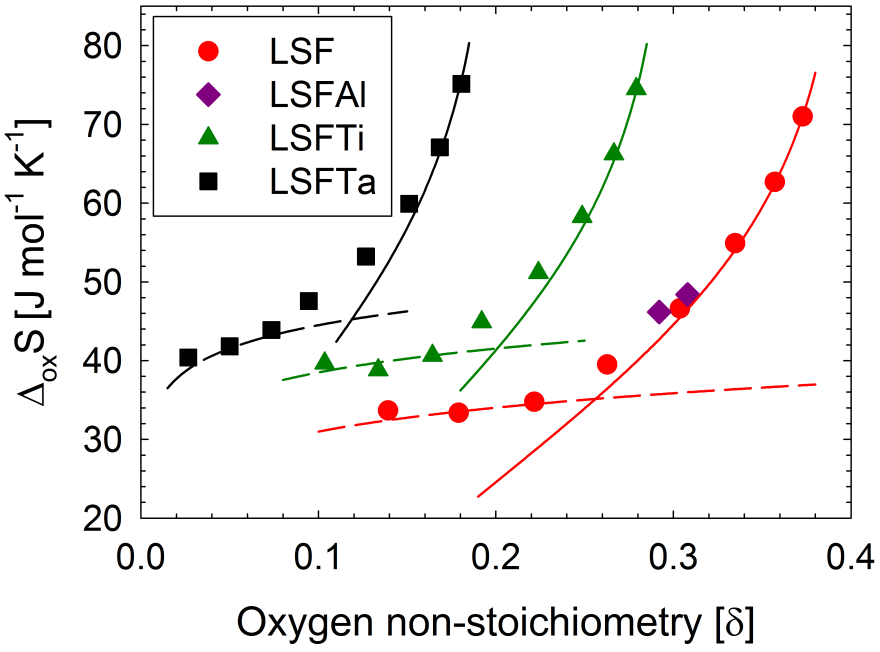

(a)

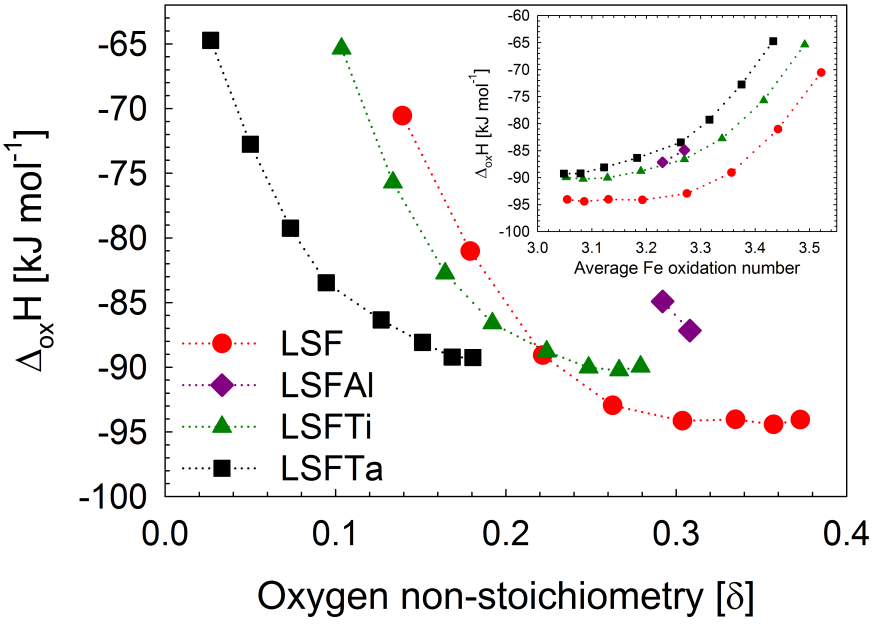

(b)

Fig. 8. (a) Partial molar entropy of oxidation as a function of oxygen non-stoichiometry. Lines are the calculated partial molar entropy according to Eq. (28) (solid) and Eq. (31) (dashed). (b) Partial molar enthalpy of oxidation as a function of oxygen non-stoichiometry. The insert show the partial molar entropy and enthalpy of oxidation as a function of average Fe oxidation number. Dotted lines are a guide to the eye.

showing a deviation from the ideal behaviour in the same region as for the partial molar entropy. The effect of this deviation on the non-stoichiometry can be seen by calculating δ and p_{O_2} from the partial molar enthalpy and entropy of oxidation using Eq. (26). This is shown for LSFTa in Fig. 9, where measured non-stoichiometry data (symbols) is presented together with calculated values from $\Delta_{ox}S$ and $\Delta_{ox}H$ (lines). The solid blue line represents values calculated from the measured partial molar enthalpy and entropy of oxidation (cf. Fig. 8). The broken red line is obtained by using the configurational entropy of the ideal point defect model (cf. solid line in Fig. 8 (a)) and a constant $\Delta_{ox}H$, corresponding to an average of the two values at $\delta > 0.16$ in Fig. 8 (b). A clear deviation from the ideal point defect model can be observed with the slope of the measured δ versus p_{O_2} being significantly steeper at high oxygen partial pressures compared to the predicted values from the ideal solution model. A similar deviation in $\Delta_{ox}H$ and $\Delta_{ox}S$ have been reported by Patrakeev et al. for $La_{0.3}Sr_{0.7}Fe_{1-x}Ga_xO_{3-\delta}$ and was attributed to a transition from localized to itinerant electrons [19]. The dashed lines in Fig. 8 (a) correspond to the partial molar entropy of oxidation calculated from Eq. (31) (model 2). This fits quite well with the experimentally obtained values for all the compositions at lower δ. Hence, the deviation from the point defect model of localized electrons at lower oxygen non-stoichiometry is attributed to a transition to itinerant electrons for all materials as δ decreases.

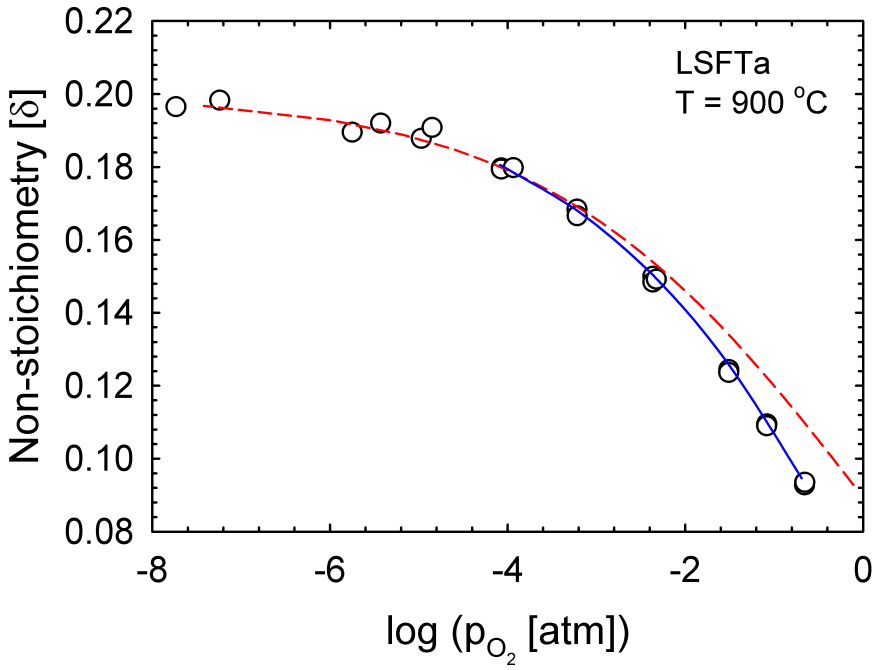

Fig. 9. Oxygen non-stoichiometry as a function of $\log p_{O_2}$ for LSFTa at 900 °C. Broken red line represents data calculated from $\Delta_{ox}H$ and $\Delta_{ox}S$ assuming ideal solution model. Solid blue line represents data calculated from measured values of $\Delta_{ox}H$ and $\Delta_{ox}S$.

The reciprocal temperature dependence of $\ln K_{ox}$ is shown in Fig. 10. A linear fit to the data was performed where the y-axis intersection and the slope define $-\Delta_{ox}H^0/R$ and $\Delta_{ox}S^0/R$, respectively, according to Eq. (25). The $\delta(p_{O_2})$ points used to fit K_{ox} for $T \neq 900\,^{\circ}\mathrm{C}$ were obtained from interpolated data points of temperature cycles at constant δ. The obtained standard enthalpy and entropy of oxidation is given in Table 4 together with reported data for similar compositions. There is a small difference in the value for the standard and partial molar entropy of oxidation, Table 4 and Fig. 8 (a), from LSF to the B-site substituted LSFAl, LSFTi and LSFTa, while the differences between the values of the three B-site substituted compositions are less significant. The calculated partial molar enthalpy of oxidation, insert in Fig. 8 (b), show a decrease in absolute value from LSF to the B-site substituted compositions when plotted against the average oxidation state of iron. The standard enthalpy of oxidation, Table 4, shows the same trend for the materials in this work as deduced by comparing to the $\Delta_{ox}H^0$ for $La_{0.2}Sr_{0.8}Fe_{0.55}Ti_{0.45}O_{3-\delta}$ reported by Park et al. [21], i.e. the absolute value decreases with substitution. A lowering of $\Delta_{ox}H$ with B-site substitution was also shown for $La_{0.3}Sr_{0.7}Fe_{1-x}Ga_xO_{3-\delta}$ by Patrakeev et al. [19]. The decrease in absolute value of the oxidation enthalpy with B-site substitution might suggest a lowering of the iron-oxygen bonding strength and hence a thermodynamic destabilisation of the perovskite phase. By partially substituting iron with a cation of higher valence the increased coulombic attraction forces between the substituted cation and the

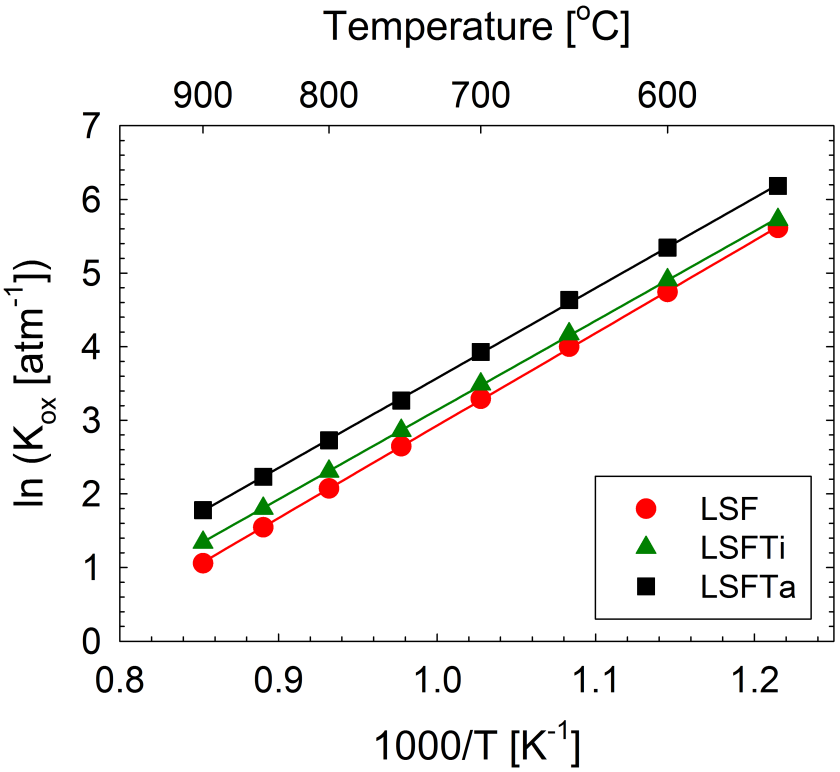

Fig. 10. Inverse temperature dependence of $\ln K_{ox}$. Standard error bars are smaller than the symbol size. Lines are linear fits to the data.

Table 4. Standard entropy and enthalpy of oxidation for different compositions. The standard error of the fit is given as the value of uncertainty.

Composition	$\Delta_{ox}S^0$ [J mol^{-1} K^{-1}]	$\Delta_{ox}H^0$ [kJ mol^{-1}]	Ref.
$La_{0.2}Sr_{0.8}FeO_{3-\delta}$	-80.1 ± 0.4	-104.5 ± 0.4	This work
$La_{0.2}Sr_{0.8}Fe_{0.8}Ti_{0.2}O_{3-\delta}$	-74.8 ± 0.4	-100.9 ± 0.4	This work
$La_{0.2}Sr_{0.8}Fe_{0.8}Ta_{0.2}O_{3-\delta}$	-71.9 ± 0.6	-101.6 ± 0.6	This work
$La_{0.2}Sr_{0.8}Fe_{0.55}Ti_{0.45}O_{3-\delta}$	-60.0*	-77.4	[21]
$La_{0.4}Sr_{0.6}FeO_{3-\delta}$	-81 ± 8	-108 ± 12	[4]
$La_{0.5}Sr_{0.5}Fe_{0.8}Ga_{0.2}O_{3-\delta}$	-66	-92	[20]

* This value is not specifically presented in the cited paper but has been calculated by extracting datapoints from a presented K_{ox} vs. $1/T$ plot

oxygen anions are expected to increase the bonding strength and hence the stability of the material. Regarding the ionic size in terms of bonding strength, substituting iron with a cation of smaller size will be expected to lead to a contraction of the unit cell yielding a shorter bond length with an increased overlap of the B-O-B bonds and hence increase the bonding strength and vice versa for substitution with a cation of larger size. The ionic radii of the different cations in this study are given in Table 2 together with the lattice constants calculated from X-ray diffraction data for the different compositions. Al^{3+} is very small and following the reasoning above, partial substitution with Al^{3+} could be expected to lead to unit cell contraction. However, this is not the case in this study as the molar volume is larger for LSFAl compared to LSF, moreover the oxidation enthalpy lower (cf. Fig. 8 (b)). Additionally, regarding the Goldschmidt tolerance factor, τ [28], which approaches unity (ideal perovskite) as the Fe on the B-site is substituted with a smaller cation, partial substitution with Al^{3+} could be expected to increase the stability of the perovskite phase. The net decrease in oxidation enthalpy with partial substitution in LSF measured in this study is therefore assigned to be mainly a lattice strain effect due to the B-site dopant's size mismatch with the substituted iron ions.

4.4 Electrical conductivity and carrier mobility

If we assume polaron hopping to be the main mechanism for electrical conductivity, Fe^{4+} and Fe^{2+} will be the majority charge carrier for p-type and n-type conductivity, respectively. By rearranging Eq. (8) and assuming that the electrical conductivity is directly proportional to the number of charge carriers in the material, we then have for a p-type conductor:

$$\sigma \propto [\mathrm{Fe}^{\bullet}_{Fe}] \propto p_{O_2}^{1/4} \tag{32}$$

Similarly we will have for an n-type conductor:

$$\sigma \propto [\mathrm{Fe}'_{Fe}] \propto p_{O_2}^{-1/4} \tag{33}$$

The electrical conductivity as a function of p_{O_2} measured at different temperatures is shown in Fig. 11 (a). The conductivity for all compositions show a p_{O_2} dependence according to Eq. (32) at 900 °C and high p_{O_2} values, which supports the assumption of p-type polaron hopping. For LSFTa the p_{O_2} power-dependence is closer to a power of 1/5 at lower temperatures, Fig. 11 (b), indicating a change in the conduction mechanism of the material. Since the total concentration of iron is greater for the unsubstituted LSF, the high conductivity may be interpreted as due to a higher concentration of charge carriers. However, as described in section 4.2, the concentration of Fe^{4+} is close to equal between the compositions and the conductivity must therefore not only be governed by the number of charge carriers alone but also by the nature of the B-site cations. The total conductivity in [S/cm] can be written as

$$\sigma = \frac{F(p\mu_p + n\mu_n + 2\delta\mu_V)}{V_m} \tag{34}$$

where F is the Faraday constant in [C/mol], V_m the molar volume in [cm^3/mol] and μ_p, μ_n and μ_V the mobilities in [$cm^2/V \cdot s$] of p-type (holes), n-type (electrons) and ionic (oxygen vacancies) charge carriers, respectively. The solid lines in Fig. 11 (a) correspond to the best fit of the conductivity data to Eq. (34) at $p_{O_2} \leq 10^{-6}$ atm assuming constant mobilities. When including the data at high p_{O_2}, where p and μ_p are dominating, the data could not be fitted under the assumption of constant mobilities. Thus, only the data at low p_{O_2} were included to decrease the effect of p and μ_p on the fitting and the data for mobility of holes, μ_p, will be treated more thoroughly later in this section. The obtained mobilities of electrons and oxygen vacancies for LSFTi and LSFTa at 900 °C is given in Table 5.The values from this study compares well with the data for $La_{0.2}Sr_{0.8}Fe_{0.55}Ti_{0.45}O_{3-\delta}$ reported by Park et al. [21], but with the oxygen vacancy mobility being slightly higher. The electron and oxygen vacancy mobilities presented in Table 5 was calculated assuming constant mobilities. Later in this section the hole-mobility is shown to vary with δ and the electron and oxygen vacancy mobilities might also be dependent on the non-stoichiometry. However, with the limited amount of data in the n-type region it is difficult to investigate this further. Hence, the mobility given in Table 5 should be regarded as approximate values.

Table 5. Mobility of electrons and oxygen vacancies at 900 °C.

	μ_n [cm^2 V^{-1} s^{-1}]	μ_V [cm^2 V^{-1} s^{-1}]	Ref.
$La_{0.2}Sr_{0.8}Fe_{0.8}Ti_{0.2}O_{3-\delta}$	$(9.6 \pm 0.2) \cdot 10^{-4}$	$(1.01 \pm 0.02) \cdot 10^{-4}$	This work
$La_{0.2}Sr_{0.8}Fe_{0.8}Ta_{0.2}O_{3-\delta}$	$(1.22 \pm 0.03) \cdot 10^{-3}$	$(9.7 \pm 0.2) \cdot 10^{-5}$	This work
$La_{0.2}Sr_{0.8}Fe_{0.55}Ti_{0.45}O_{3-\delta}$	$1.8 \cdot 10^{-3}$	$3.9 \cdot 10^{-5}$	[21]

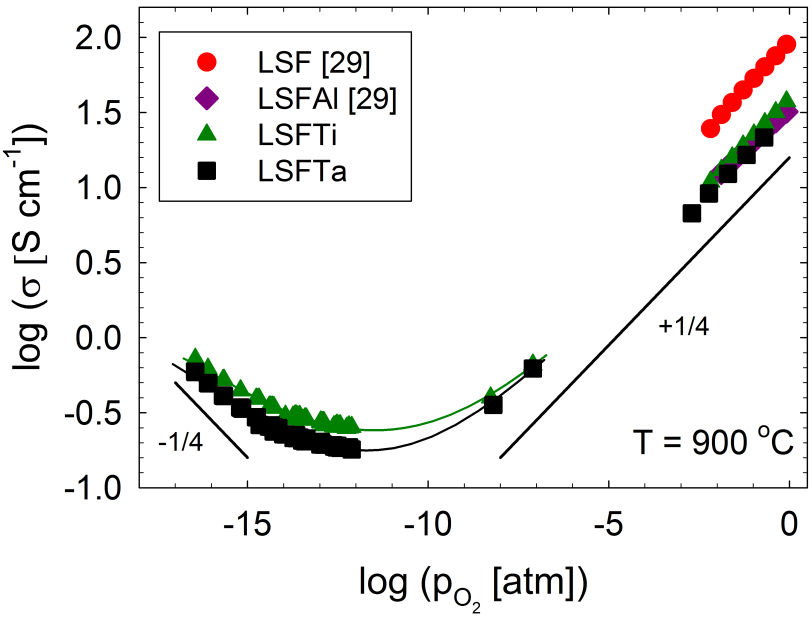

(a)

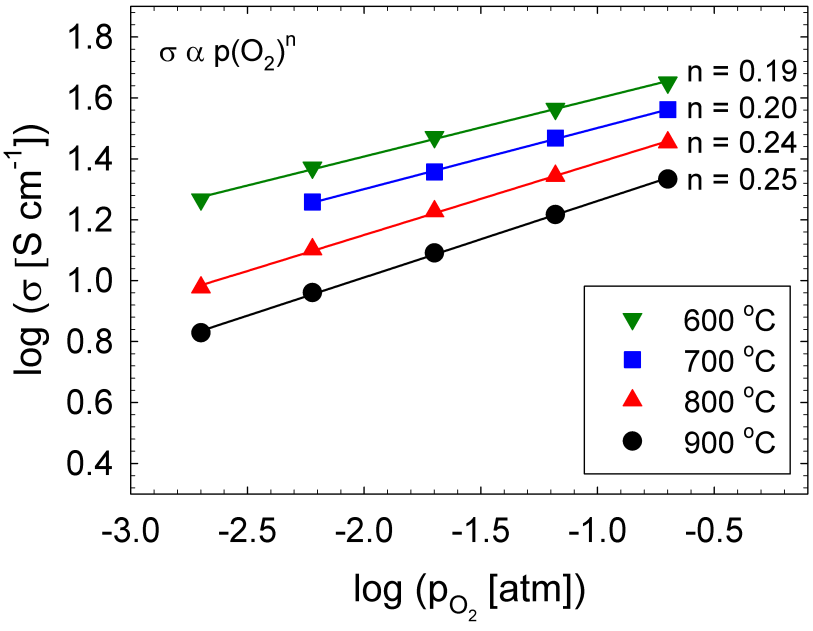

(b)

Fig. 11. (a) The total conductivity of LSFB. Data for LSF and LSFAl taken from [29]. $p_{O_2}^{1/4}$ and $p_{O_2}^{-1/4}$ guide lines are added for reference. Solid lines are least square fits of the data to Eq. (34) (b) The conductivity as a function of p_{O_2} at different temperatures for LSFTa. Lines are linear fits to the data. $p_{O_2}^{1/4}$ and $p_{O_2}^{1/5}$ guide lines are added for reference.

The partial conductivity and self-diffusion coefficient of a species i can be calculated from the mobility of the species, viz [30]:

$$\sigma_i = \frac{c_i z_i F}{V_m} \mu_i \tag{35}$$

$$D_i = \frac{RTV_m}{c_i (z_i F)^2} \sigma_i \tag{36}$$

where c_i is the concentration of the species [mol/mol] and z_i is the charge of the species i. The ionic conductivity, $\sigma_{O^{2-}}$, vacancy self diffusion coefficient, D_V and oxygen self-diffusion coefficient, D_O, have been calculated by using Eq. (35) and (36) and are summarized in Table 6. D_V obtained by electrical conductivity relaxation for LSFTi and LSFTa at 900 °C have been reported as $7.02 \cdot 10^{-6}$ cm^2/s and $9.08 \cdot 10^{-6}$ cm^2/s, respectively [31], which compare quite well with those calculated from the coulometric titration and conductivity measurements in this study. A more thorough discussion on ionic conductivity and diffusion coefficients for the materials in this study can be found elsewhere [31]. Also the values found here is close to the value reported for $La_{0.6}Sr_{0.4}FeO_{3-\delta}$ in [14].

Table 6. Ionic conductivity and vacancy self-diffusion coefficients at 900 °C.

	$\sigma_{O^{2-}}$ [S cm^{-1}]	D_V [cm^2 s^{-1}]	D_O [cm^2 s^{-1}]	Ref.
8% YSZ	$9.42 \cdot 10^{-1}$	-	-	[32]
$La_{0.2}Sr_{0.8}Fe_{0.8}Ti_{0.2}O_{3-\delta}$	$1.57 \cdot 10^{-1}$	$5.11 \cdot 10^{-6}$	$5.67 \cdot 10^{-7}$	This work
$La_{0.2}Sr_{0.8}Fe_{0.8}Ta_{0.2}O_{3-\delta}$	$9.86 \cdot 10^{-2}$	$4.90 \cdot 10^{-6}$	$3.50 \cdot 10^{-7}$	This work
$La_{0.2}Sr_{0.8}Fe_{0.55}Ti_{0.45}O_{3-\delta}$	$3.5 \cdot 10^{-2}$	-	-	[21]
$La_{0.6}Sr_{0.4}FeO_{3-\delta}$	-	$4.4 \cdot 10^{-6}$	-	[14]

At high p_{O_2} we have $p \gg n$ and by assuming $\mu_p \gg \mu_{V_O^{\bullet\bullet}}$ Eq. (34) can be simplified to

$$\sigma = \frac{F}{V_m} p \mu_p \tag{37}$$

and p can be calculated according to Eq. (15). The hole mobility calculated from Eq. (37) as a function of δ is shown in Fig. 12 (a). There is a clear difference in the mobility between LSF and the B-site substituted compositions LSFTi and LSFTa which reflects the differences in conductivity. However, the difference in mobility between LSFTi and LSFTa is rather insignificant. The hole mobility is not independent of δ, but increase with the oxygen content, or in terms of electronic defects with increasing amounts of Fe^{4+}. It can clearly be seen in the case of LSFTa that the δ dependence is stronger at lower temperatures. The effect of the variable mobility on the conductivity can be seen in Fig. 12 (b) where the conductivity at 900 °C is presented as a function of the concentration of Fe^{4+}. The solid lines represent a model introduced by Søgaard et al. [14], corresponding to the best fit to Eq. (37) with

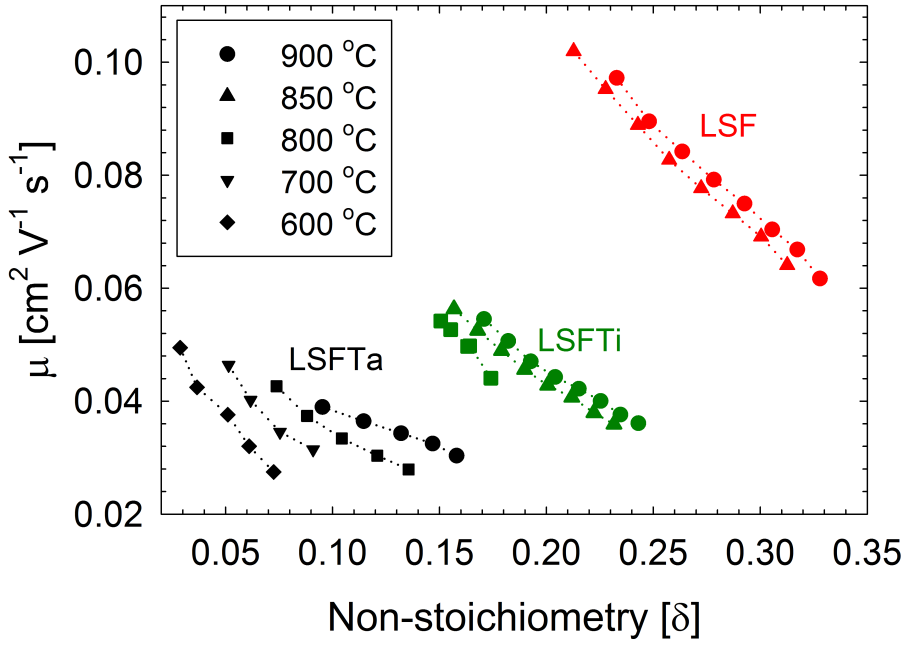

(a)

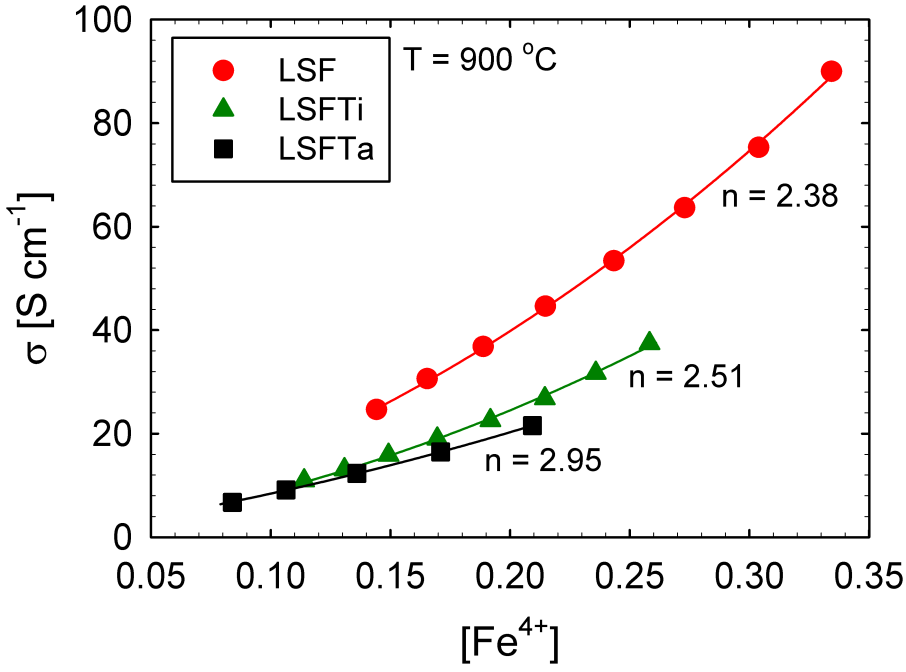

(b)

Fig. 12. (a) Hole mobility as a function of δ. Dotted lines are guide to the eye. (b) Conductivity as a function of concentration of Fe^{4+} at 900 °C. Solid lines are best fit to the model presented in section 4.4 with the corresponding fitting parameter, n, given for each plot.

μ_p assumed proportional to $([\mathrm{Fe}_{\mathrm{Fe}}^{\mathrm{x}}] - n\delta) \cdot [\mathrm{O}_{\mathrm{O}}^{\mathrm{x}}]$, where n is a fitting parameter. The fitting parameter, n, equals 2.38, 2.51 and 2.95 for LSF, LSFTi and LSFTa, respectively, and the model fit very well with the experimental data. A variable μ_p with the oxygen content have also been reported for $La_{0.3}Sr_{0.7}Fe_{1-x}Ga_xO_{3-\delta}$ ($0 \leq x \leq 0.4$) [15, 19] and $La_{0.4}Sr_{0.6}FeO_{3-\delta}$ [14]. Patrakeev et al. proposed the mobility dependency on δ to possibly be due to the change in concentration of Fe–O–Fe bonds. This is the responsible pathway for the polaron conduction in perovskites and will yield a linear δ-dependency of μ_p. However, the mobilities presented in Fig. 12 (a) show a small non-linearity, especially for LSFTa, and do also not show a direct proportionality with the concentration of δ (i.e. concentration of Fe–O–Fe bonds). In addition, the magnitude of the decrease in mobility with B-site substitution is not consistent with the change in non-stoichiometry, and thus the magnitude of decrease in Fe–O–Fe bonds. Consequently, the differences and relationships in mobility can not be solely explained by the concentration of polaron pathways. A non-linear relationship between mobility and δ may arise from an increased overlap of iron and oxygen orbitals as the unit cell contracts for decreasing δ. This is suggested to be a significant reason for the mobility dependency on δ observed for LSF, LSFTi and LSFTa. The difference in hole mobility between the compositions might also partly be an effect of a decreased orbital overlap accompanied by the molar volume increase with B-site substitution (cf. Table 2). An increased overlap of the oxygen and iron orbitals at decreasing δ, yielding a more delocalized behaviour [33], fits well with the proposed scheme for the oxygen thermodynamics as discussed in section 4.3.

5 Conclusions

The oxygen non-stoichiometry of the materials $La_{0.2}Sr_{0.8}Fe_{0.8}B_{0.2}O_{3-\delta}$, B = Fe, Al, Ti, Ta, as a function of temperature and oxygen partial pressure was determined by coulometric titration and thermogravimetric analysis. A large difference in the non-stoichiometry between the different compositions was shown and the main mechanism for charge compensation with B-site substitution at high temperature was shown to be ionic compensation. Thermodynamic quantities were extracted from the coulometric titration data and showed the configurational entropy to deviate from the localized electron model with decreasing oxygen non-stoichiometry. The deviation could be explained by a transition to itinerant electrons with decreasing non-stoichiometry. The oxidation enthalpy showed a decrease in absolute value with B-site substitution, suggesting a lowering of the B-O-B bonding strength and thermodynamic destabilization. This was assigned to an effect of increased lattice strain due to size mismatch between the substituted iron ions and the B-site dopants. Thus the effect of lattice strain on the thermodynamic stability is larger than the expected increase in stability from increased coulombic interaction forces by B-site substitution with a high valent cation.

The electrical conductivity as a function of temperature and partial pressure of oxygen was determined by a four-probe DC method. The p-type conductivity was shown to decrease with B-site substitution due to a decrease in charge carrier mobil-

ity. The hole mobility was shown to increase with δ, presumably due to an increase in the concentration of Fe-O-Fe bonds and a larger overlap between iron and oxygen ion orbitals at decreasing δ. The hole mobility was also shown to decrease with B-site substitution due to a combined effect of coulombic interaction forces and an increased molar volume yielding lower overlap between the iron and oxygen ion orbitals.

Acknowledgment

Funding provided by the Norwegian Research Council (NFR), FRINAT-project no. 191358: The kinetics of surface exchange reactions in oxide based mixed conductors at reducing conditions and high temperatures, is acknowledged. The author would like to acknowledge the collaboration with Prof. Henny J.M. Bouwmeester and Tan Nhut Phung at the University of Twente and their helpful inputs and discussions.

References

[1] H. J. M. Bouwmeester, Dense ceramic membranes for methane conversion, Catalysis Today 82 (1-4) (2003) 141–150.

[2] J. B. Goodenough, Electronic and ionic transport properties and other physical aspects of perovskites, Reports on Progress in Physics 67 (11) (2004) 1915–1993.

[3] M. Mogensen, D. Lybye, N. Bonanos, P. V. Hendriksen, F. W. Poulsen, Factors controlling the oxide ion conductivity of fluorite and perovskite structured oxides, Solid State Ionics 174 (1-4) (2004) 279–286.

[4] J. Mizusaki, M. Yoshihiro, S. Yamauchi, K. Fueki, Nonstoichiometry and defect structure of the perovskite-type oxides $La_{1-x}Sr_xFeO_{3-\delta}$, Journal of Solid State Chemistry 58 (2) (1985) 257–266.

[5] Y. Teraoka, H. M. Zhang, S. Furukawa, N. Yamazoe, Oxygen Permeation through Perovskite-type Oxides, Chemistry Letters (11) (1985) 1743–1746.

[6] V. V. Kharton, E. V. Tsipis, A. A. Yaremchenko, I. P. Marozau, A. P. Viskup, J. R. Frade, E. N. Naumovich, Oxygen permeability, electronic conductivity and stability of $La_{0.3}Sr_{0.7}CoO_3$-based perovskites, Materials Science and Engineering B: Solid-State Materials for Advanced Technology 134 (1) (2006) 80–88.

[7] L. W. Tai, M. M. Nasrallah, H. U. Anderson, Thermochemical Stability, Electrical Conductivity, and Seebeck Coefficient of Sr-Doped $LaCo_{0.2}Fe_{0.8}O_{3-\delta}$, Journal of Solid State Chemistry 118 (1) (1995) 117–124.

[8] F. J. Berry, J. F. Marco, X. Ren, Reduction properties of phases in the system $La_{0.5}Sr_{0.5}MO_3$ (M=Fe, Co), Journal of Solid State Chemistry 178 (4) (2005) 961–969.

[9] S. E. Dann, D. B. Currie, M. T. Weller, M. F. Thomas, A. D. Al-Rawwas, The Effect of Oxygen Stoichiometry on Phase Relations and Structure in the System $La_{1-x}Sr_xFeO_{3-\delta}$ ($0 < x < 1$, $0 < \delta < 0.5$), Journal of Solid State Chemistry 109 (1) (1994) 134–144.

[10] Ø. F. Lohne, J. Gurauskis, T. N. Phung, M. A. Einarsrud, T. Grande, H. J. M. Bouwmeester, K. Wiik, Effect of B-site substitution on the stability of $La_{0.2}Sr_{0.8}Fe_{0.8}B_{0.2}O_{3-\delta}$, B = Al, Ga, Cr, Ti, Ta, Nb, Solid State Ionics 225 (2012) 186–189, Paper 2 in this thesis.

[11] Y. Teraoka, T. Nobunaga, N. Yamazoe, Effect of cation substitution on the oxygen semipermeability of perovskite-type oxides, Chemistry Letters (3) (1988) 503–506.

[12] S. Diethelm, D. Bayraktar, T. Graule, P. Holtappels, J. Van herle, Improved stability of $La_{0.5}Sr_{0.5}FeO_3$ by Ta-doping for oxygen separation membrane application, Solid State Ionics 180 (11-13) (2009) 857–860.

[13] J. Cheng, A. Navrotsky, X. D. Zhou, H. U. Anderson, Thermochemistry of $La_{1-x}Sr_xFeO_{3-\delta}$ solid solutions ($0.0 \leq x \leq 1.0$, $0.0 \leq \delta \leq 0.5$), Chemistry of Materials 17 (8) (2005) 2197–2207.

[14] M. Søgaard, P. Vang Hendriksen, M. Mogensen, Oxygen nonstoichiometry and transport properties of strontium substituted lanthanum ferrite, Journal of Solid State Chemistry 180 (4) (2007) 1489–1503.

[15] M. V. Patrakeev, I. A. Leonidov, V. L. Kozhevnikov, K. R. Poeppelmeier, p-type electron transport in $La_{1-x}Sr_xFeO_{3-\delta}$ at high temperatures, Journal of Solid State Chemistry 178 (3) (2005) 921–927.

[16] J. Mizusaki, M. Yoshihiro, S. Yamauchi, K. Fueki, Thermodynamic quantities and defect equilibrium in the perovskite-type oxide solid solution $La_{1-x}Sr_xFeO_{3-\delta}$, Journal of Solid State Chemistry 67 (1) (1987) 1–8.

[17] I. A. Leonidov, V. L. Kozhevnikov, M. V. Patrakeev, E. B. Mitberg, K. R. Poeppelmeier, High-temperature electrical conductivity of $Sr_{0.7}La_{0.3}FeO_{3-\delta}$, Solid State Ionics 144 (3-4) (2001) 361–369.

[18] J. Yoo, A. Verma, S. Wang, A. J. Jacobson, Oxygen transport kinetics in $SrFeO_{3-\delta}$, $La_{0.5}Sr_{0.5}FeO_{3-\delta}$, and $La_{0.2}Sr_{0.8}Cr_{0.2}Fe_{0.8}O_{3-\delta}$ measured by electrical conductivity relaxation, Journal of the Electrochemical Society 152 (3) (2005) A497–A505.

[19] M. V. Patrakeev, E. B. Mitberg, A. A. Lakhtin, I. A. Leonidov, V. L. Kozhevnikov, V. V. Kharton, M. Avdeev, F. M. B. Marques, Oxygen nonstoichiometry, conductivity, and Seebeck coefficient of $La_{0.3}Sr_{0.7}Fe_{1-x}Ga_xO_{2.65+\delta}$ perovskites, Journal of Solid State Chemistry 167 (1) (2002) 203–213.

[20] J. Yoo, A. J. Jacobson, Measurements of electrical conductivity and oxygen nonstoichiometry of $La_{0.5}Sr_{0.5}Ga_{0.2}Fe_{0.8}O_{3-\delta}$ using gastight electrochemical cells, Journal of the Electrochemical Society 156 (9) (2009) B1085–B1091.

[21] C. Y. Park, A. J. Jacobson, Electrical conductivity and oxygen nonstoichiometry of $La_{0.2}Sr_{0.8}Fe_{0.55}Ti_{0.45}O_{3-\delta}$, Journal of the Electrochemical Society 152 (7) (2005) J65–J73.

[22] B. T. Dalslet, M. Søgaard, H. J. M. Bouwmeester, P. V. Hendriksen, Defect chemistry and oxygen transport of $(La_{0.6}Sr_{0.4-x}M_x)_{0.99}Co_{0.2}Fe_{0.8}O_{3-\delta}$, M = Ca (x = 0.05, 0.1), Ba (x = 0.1, 0.2), Sr. Part I: Defect chemistry, Solid State Ionics 180 (20-22) (2009) 1173–1182.

[23] I. Yasuda, T. Hikita, Precise determination of the chemical diffusion coefficient of calcium-doped lanthanum chromites by means of electrical conductivity relaxation, Journal of the Electrochemical Society 141 (5) (1994) 1268–1273.

[24] F. A. Kröger, H. J. Vink, Relations between the Concentrations of Imperfections in Crystalline Solids, Solid State Physics 3 (C) (1956) 307–435.

[25] E. Bakken, T. Norby, S. Stølen, Redox energetics of perovskite-related oxides, Journal of Materials Chemistry 12 (2) (2002) 317–323.

[26] J. Mizusaki, S. Yamauchi, K. Fueki, A. Ishikawa, Nonstoichiometry of the perovskite-type oxide $La_{1-x}Sr_xCrO_{3-\delta}$, Solid State Ionics 12 (C) (1984) 119–124.

[27] R. D. Shannon, Revised effective ionic-radii and systematic studies of interatomic distances in halides and chalcogenides, Acta Crystallographica Section A 32 (SEP1) (1976) 751–767.

[28] V. M. Goldschmidt, L. Thomassen, E. Ulrich, T. F. W. Barth, G. O. J. Lunde, D. Holmsen, W. H. Zachariasen, Geochemische verteilungsgesetze der elemente, Norsk videnskaps-akademi l Oslo. Skrifter. I. Mathematisk-naturvidenskabelig klasse, 1923,no. 3; 1924,no. 4-5; 1925,no. 5, 7: 1926,no. 1-2, 8, In kommission bei J. Dybwad, I kommission hos J. Dybwad, Kristiania, : Oslo, 1923.

[29] T. N. Phung, Unpublished work, Ph.D. thesis (2013).

[30] W. Gao, N. Sammes, An introduction to electronic and ionic materials, World Scientific, Singapore, 1999.

[31] Ø. F. Lohne, Oxygen transport properties of B-site substituted Lanthanum strontium ferrites assessed by electrical conductivity relaxation, Paper 4 in this thesis.

[32] S. P. S. Badwal, Zirconia-based solid electrolytes: microstructure, stability and ionic conductivity, Solid State Ionics 52 (1-3) (1992) 23–32.

[33] N. Ramadass, ABO_3-type oxides – Their structure and properties – A bird's eye view, Materials Science and Engineering 36 (2) (1978) 231–239.